
MACHINE LEARNING BASED MEDICAL IMAGE DEEPPFAKE DETECTION: A COMPARATIVE STUDY

Siddharth Solaiyappan
Northwood High School
Irvine Unified School District
Irvine, CA 92620
solaiyappan@chapman.edu

Yuxin Wen
Fowler School of Engineering
Chapman University
Orange, CA 92866
yuwen@chapman.edu

ABSTRACT

Deep generative networks in recent years have reinforced the need for caution while consuming various modalities of digital information. One avenue of deepfake creation is aligned with injection and removal of tumors from medical scans. Failure to detect medical deepfakes can lead to large setbacks on hospital resources or even loss of life. This paper attempts to address the detection of such attacks with a structured case study. We evaluate different machine learning algorithms and pretrained convolutional neural networks on distinguishing between tampered and untampered data. The findings of this work show near perfect accuracy in detecting instances of tumor injections and removals.

Keywords Computed Tomography, Generative Adversarial Networks, Deepfake, DICOM, Tumor, Machine Learning

1 Introduction

Computed Tomography (CT) is a medical imaging technique used to create image records of tissue, bones and blood vessels. The scan is generated as a collection of narrow X-ray beams are projected onto a subject, creating cross sectional images of the region of interest. Collections of two dimensional cross sections are then digitized into a three dimensional volume, allowing for views of the target from multiple angles (T. et al., 2021). Other medical imaging modalities such as Magnetic Resonance Imaging (MRI), functional MRI, and ultrasound, are not addressed in this paper. Industry standard for CT scan storage is the Digital Imaging and Communications in Medicine (DICOM), popular for its compatibility with the Picture and Archive Communication System (PACS). PACS servers allow ease of transfer of medical imagery between hospital scanners, radiologists workstations, and network intermediates. Medical centers are often equipped with outdated security measures and legacy software, allowing for open access to data. For example, researchers from McAfee equipped with 3D printers reconstructed a model of a pelvis from unsecured volumetric DICOM data (Beck, 2018). This vulnerability also allows attackers to tamper scans once extracted from the server.

Copy-move and image splicing are two common image tampering methods. Copy-move involves duplicating an area of non-interest over the target region, masking the region of interest from the viewer. This method can also be used to duplicate the target region and increase the frequency of regions of interest. The typical downside of copy-move involves mimicking image properties across regions such as, hue, brightness, noise, etc. Such drawbacks make this method impractical to tamper volumetric data modalities, which require convincing tampering from various viewing angles. Algorithmic and deep learning approaches to copy-move detection have been conducted by other researchers (Bunk et al., 2017; Cozzolino et al., 2015; Meena and Tyagi, 2020). Image-splicing closely follows the procedure of copy-move, however, the duplicated area of interest originates from an external image. This method has the same downsides as the former, and deep learning approaches to splicing detection have been implemented (Rao and Ni, 2016; El-Latif et al., 2020).

Pix2pix (Isola et al., 2016) is a software developed by Isola et al. that focuses on synthesizing images by learning their input/output mappings, as well as the respective loss functions for training the mapping. In 2019, Mirsky et al. at Ben Gurion University developed CT-GAN (Mirsky et al., 2019): a pix2pix (Isola et al., 2016) based generative adversarial network framework capable of adding or removing cancer tumors from a patient’s CT lung scans. These tampered scans were later subjected to three professional radiologists and AI screening. The authors of (Mirsky et al., 2019) selected three radiologists, each with 2, 5, and 7 years of experience respectively, to diagnose a batch of scans with, and without tampering. This experiment was conducted through 2 distinct trials: blind and open. In the blind trial, the scan samples were provided to the radiologists with no knowledge of tampering. The results of the blind trial showed 99% of tumor injected scans were misdiagnosed as malignant, and 94% of tumor removed scans were misdiagnosed as benign. Once aware of the tampering mechanisms in an open trial, the misdiagnosis rates were 60% and 87% respectively. Also added as an AI detector was the winner of the 2017 Kaggle Data Science Bowl: a 1 million dollar competition for lung cancer detection (Liao et al., 2017). (Mirsky et al., 2019) verified this AI misdiagnosed 100% of tampered scans. The nature of tampering using generative networks are clearly convincing, and indicate a higher degree of realism than generic tampering methods.

80 million CT scans are conducted in the U.S. every year (School, 2020). With this frequency of medical imaging, deceptive attacks of added tumors can cause patients to receive unnecessary treatment, costing millions of dollars in hospital resources. Removing a tumor will deprive the patient of needed treatment and severely advance an existing condition, or even lead to loss of life. Incentives for such attacks can be politically motivated, financially motivated in the case of a ransom, insurance fraud, or even murder.

Digital watermarking and equivalence checking are current methods of tamper prevention and detection. Digital watermarking is the conventional standard of ensuring security in medical imaging, though periodically criticized for reducing image quality or important image features. Recent works with watermarking have addressed salt and pepper noise, filter noise, gaussian noise, gemma correction, and motion blur tampering methods using discrete wavelet transform (DWT) and singular value decomposition (SVD) (Savaridass et al., 2021; Mohammed et al., 2021). However, watermarking studies addressing deep generative tampering have yet to be conducted. Rather than addressing tampering at the image level, equivalence checking attempts to match each scan’s origin and destination in a PACS network through a certain established algebraic equivalence (Brunese et al., 2019). Though effective when the raw scan is replaced with a tampered version, GAN-based tampering in real-time is yet to be tested with equivalence checking. With the introduction of medical deepfakes being so novel, no detection mechanisms have been tested to mitigate the effects. As a result, we propose machine learning approaches to detect tampering by the CT-GAN framework (Mirsky et al., 2019).

The contents of this paper are organized as follows: Section 2 addresses dataset information and model details, Section 3 demonstrates experiments addressing different sub-tasks and results describing detector performance.

2 Materials and Methods

All the data used in this study is from the LIDC-IDRI dataset (Armato III et al., 2015; SG et al., 2011) (untampered) from The Cancer Imaging Archive (Clark et al., 2013), and the CT-GAN dataset (tampered) (Mirsky et al., 2019; Dua and Graff, 2017). All scans are patient records in DICOM format, separated by uniquely labeled folders that correspond to patient ID.

The dataset can be grouped into three categories:

- Untampered - Natural scans with or without cancerous growth
- False Benign (FB) - Scan with artificially removed cancerous growth
- False Malign (FM) - Scan with artificially injected cancerous growth

Data in the tampered dataset is organized into patient records from the blind trial (radiologists evaluated 80 3D volumes without knowledge of tampering) and open trial (radiologists evaluated 20 3D volumes with knowledge of tampering). These segmentations will be used as the train set and test set for the tampered class, and will stay constant throughout sections. Train-test split ratio is 85:15. Table 1 lists quantities of available training images.

Each section evaluates the data on various preprocessing techniques, machine learning algorithms (Support Vector Machine, Random Forest, Decision Tree) (Pedregosa et al., 2011), and transfer learning convolutional neural networks with Keras (DenseNet121, DenseNet201, ResNet50, ResNet101, VGG19). All neural networks follow the same architecture of a convolution base, a dense 10-neuron layer with rectified linear activation (ReLU), and a softmax activated 2-neuron layer. All pretrained convolution layers were frozen while other layers were allowed to train.

Table 1: Number of training images by type

Untampered	FB	FM	Total
2278	61	34	2373

3 Experiments and Results

Section 3.1 addresses FM image detection using raw, localized, and augmented images. Section 3.2 addresses FB image detection using delocalized, and augmented images. Section 3.3 addresses multiclass classification of delocalized data augmented images.

3.1 False Malign detection

The primary focus of this section is detecting False Malign from untampered scans. In the blind trial conducted by the authors of CT-GAN (Mirsky et al., 2019), 3 radiologists and an AI were asked to classify 80 scans as either benign or malignant. The injected tumor misdiagnosis rate for radiologists and AI was 99.2% and 100% respectively. The AI model used was a 3D Deep Leaky Noisy-or Network (Liao et al., 2017) trained on the Lung Nodule Analysis (LUNA) dataset (Setio et al., 2016).

3.1.1 Raw Image Classification

Authors of CT-GAN (Mirsky et al., 2019), and (A. P. Reeves, 2011), have provided annotations to voxel coordinates of tumor sites and nodule locations in the tampered and untampered datasets respectively. Figure 1 shows annotated 2D slices extracted from the corresponding 3D scans. Tampered regions are circled. We first conduct the classification using raw images.

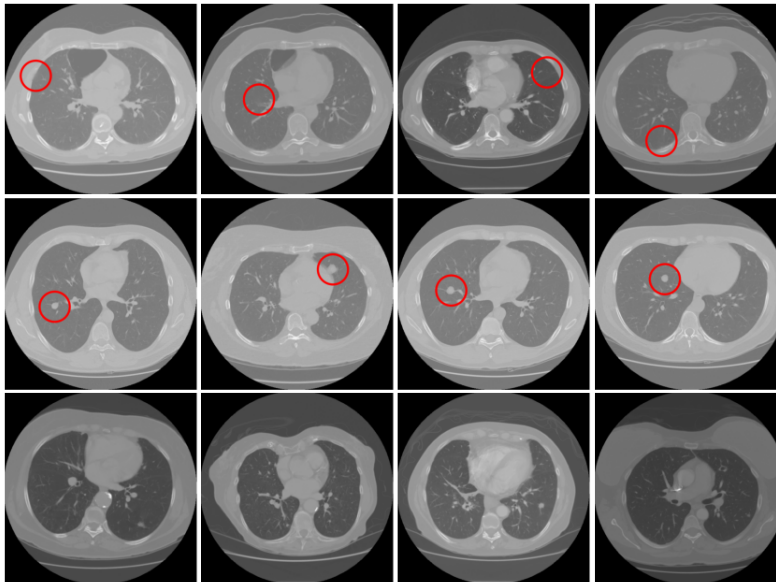


Figure 1: Raw CT scan images with tampered regions circled

Row 1: FB samples, Row 2: FM samples, Row 3: Untampered samples

The eight models are trained without data preprocessing on all tampered images, and a subset of untampered images to balance data quantity for classes. Table 2 shows train and test metrics for the classifiers. Insufficient data severely hindered neural network accuracy due to overfit. Figure 2 shows the receiver operator characteristic (ROC) curves, where TPR and FPR represent true positive rate and false positive rate respectively. ResNet101 is able to reach 80% TPR with the hindrance of a 50% FPR rate and would be considered poor (El Khouli et al., n.d.). FPR addresses

classification accuracy of tampered scans and is required to be minimized as much as possible in order to avoid life threatening misclassification. Given low quantity high dimensional data, the bootstrap aggregation and random feature selection allow for high random forest performance. However with limited test sample presence, further testing is required to determine true accuracy levels with features at scale.

Table 2: Classifier performance no image preprocessing

Classifier	Train Accuracy	Train Loss	Test Accuracy	Test Loss
SVM	0.98	-	0.95	-
Random Forest	1	-	0.95	-
Decision Tree	0.96	-	0.95	-
DenseNet121	0.82	0.38	0.54	1.58
DenseNet201	0.86	0.34	0.57	1.27
ResNet50	0.99	0.08	0.56	0.58
ResNet101	0.98	0.11	0.61	1.05
VGG19	0.98	0.11	0.43	1.62

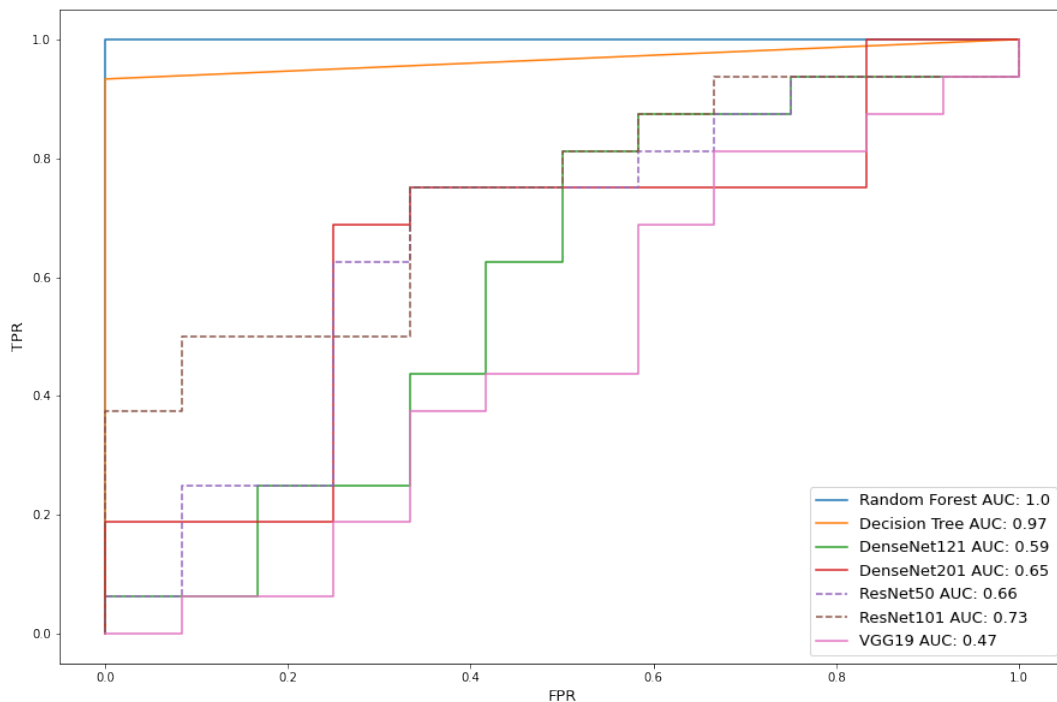


Figure 2: Classifier ROC curves without image preprocessing

3.1.2 Tumor Site Localization

Data from the blind experiment showed radiologists can identify the locations of tumor sites, however, the challenge was distinguishing between natural and artificially generated tumors. We test localizing the tumor site in an attempt to mimic this difficulty. The annotated coordinate data from the dataset allows for tumor site localization: slicing a 128x128 figure from the generated pixel array using the tumor site as center. This section uses the same scans as 3.1.1, but localizes the scans to create the new dataset. FB scans will still be used for training as annotated locations of tumor sites are provided. However, practical use of the models are restricted to FM scan detection as FB site locations will be unknown to detection mechanisms and cannot be localized. Examples of localized images are shown in Figure 3.

Table 3 indicates region of interest (ROI) extraction increased classifier accuracy for all model types. Due to a decrease in number of learnable features, and reasons previously mentioned, random forest and support vector machines

both reach perfect accuracy with small testing samples. In terms of deep learning, Figure 4 shows VGG19 can achieve a 75% true positive rate with a 45% false positive rate, and ResNet101 can achieve a 90% TPR with a 35% FPR dependence. Though deep learning accuracy increased, the scores indicate little deviation from guessing accuracy for a binary classifier

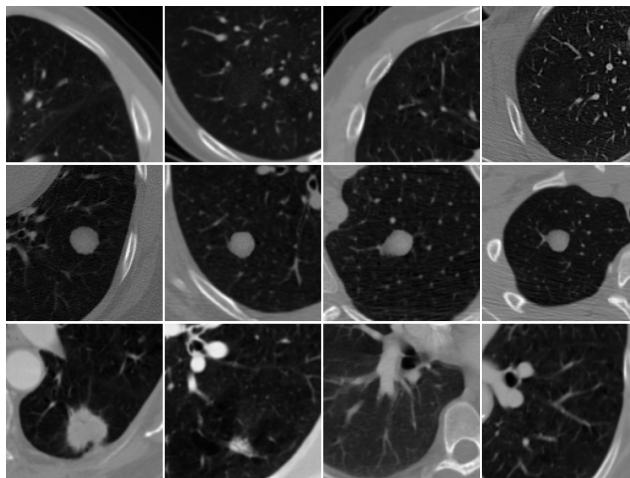


Figure 3: Examples of localized images

Row 1: FB samples, Row 2: FM samples, Row 3: Untampered samples

Table 3: Localized image classifier performance

Classifier	Train Accuracy	Train Loss	Test Accuracy	Test Loss
SVM	0.97	-	1	-
Random Forest	1	-	1	-
Decision Tree	1	-	0.98	-
DenseNet121	1	0.13	0.63	0.87
DenseNet201	1	0.02	0.64	1.08
ResNet50	1	0.07	0.67	0.92
ResNet101	1	0.03	0.63	1
VGG19	0.79	0.5	0.71	0.78

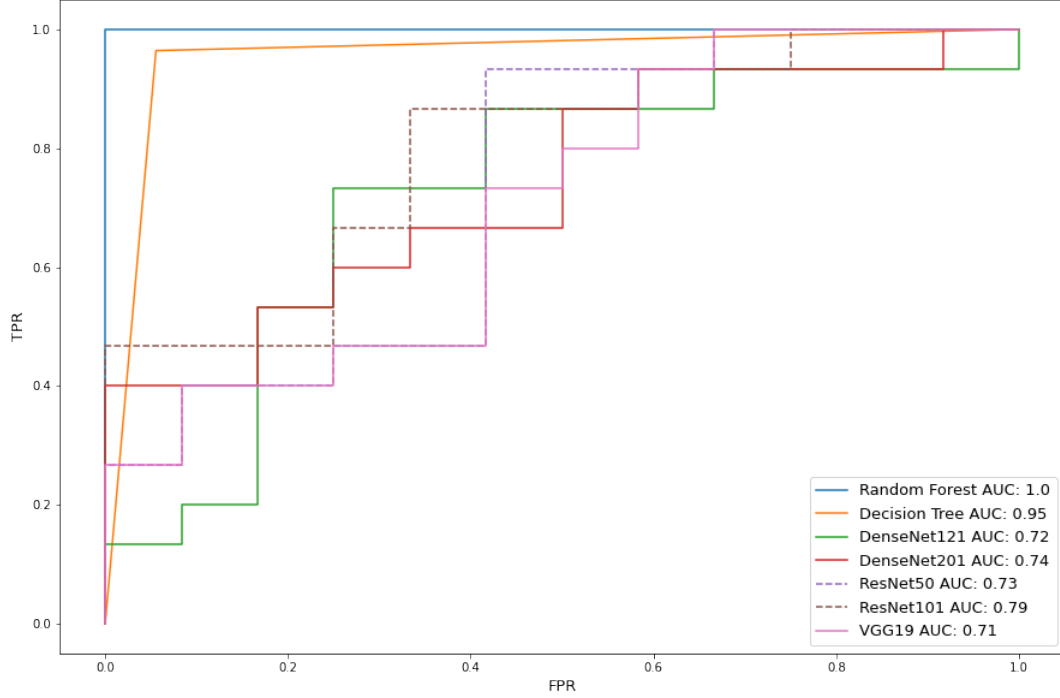


Figure 4: Localized image classifier ROC Curves

3.1.3 Data Augmentation

The effects of data quality and quantity in medical applications have been studied (Barragán-Montero et al., 2021). Higher performance was established with increase in data quality, but negligible changes were detected with increase in dataset size. The possibility of generating high quality data via CT-GAN (Mirsky et al., 2019) was deemed impractical due to the algorithm’s demanding hardware dependencies. As such, with the current objective of increasing specifically deep learning model accuracy, we reconduct the localized tumor site test with data augmentation for both classes. The technique used closely resembles that used to augment and train CT-GAN (Mirsky et al., 2019), but in one less dimension:

- Flip over x-axis, y-axis, and both axes
- Combinations of x,y shifts; 4 units in specified direction
- Rotation of 360 degrees in 6 degree increments

Table 4: Augmented localized image classifier performance

Classifier	Train Accuracy	Train Loss	Test Accuracy	Test Loss
Support Vector Machine	0.984	-	0.978	-
Random Forest	1	-	0.979	-
Decision Tree	1	-	0.925	-
DenseNet121	0.995	0.03	0.991	0.042
DenseNet201	0.991	0.026	0.987	0.077
ResNet50	0.995	0.03	0.991	0.022
ResNet101	0.989	0.029	0.98	0.06
VGG19	0.977	0.995	0.949	0.547

Table 4 shows the addition of data allowed near perfect score improvement in terms of transfer learning. However, the increase in sample size decreased overall ML algorithm accuracy due to a higher possibility for false predictions.

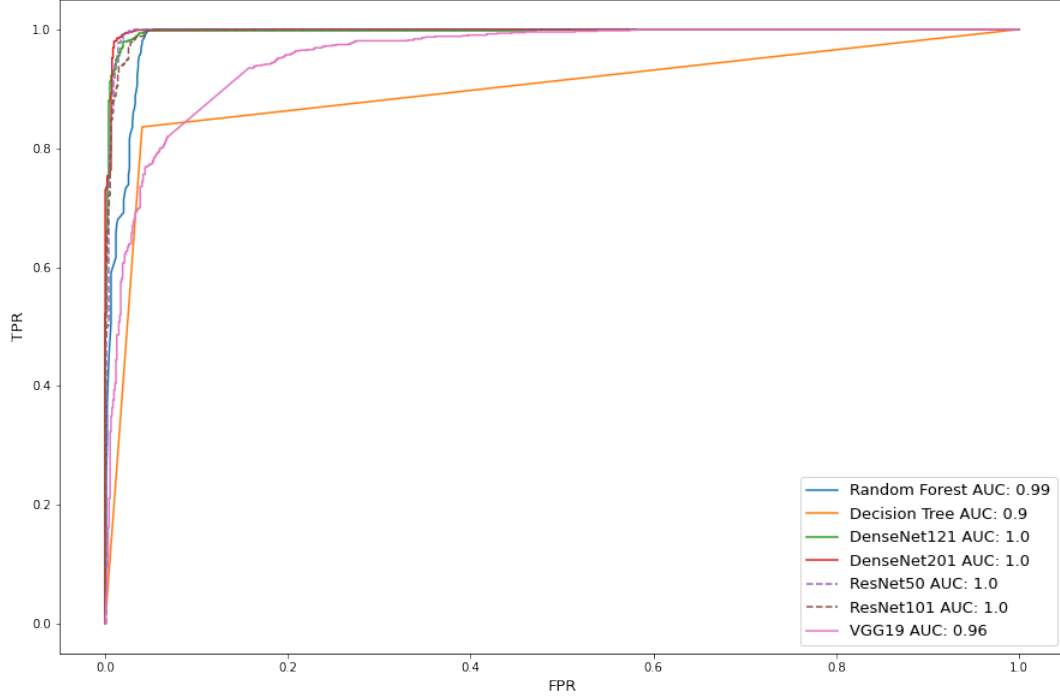


Figure 5: Augmented localized ROC curves

This phenomenon is also reflected in Figure 5 as deep learning reached AUC scores nearing 1.0, while the Decision Tree AUC score dropped 0.05 from Figure 4.

In this section, we showed it is in fact possible to detect tumor injected cancer scans, despite the failed efforts of radiologists, and their accompanying AI tools, to do the same. In the open trials of the CT-GAN (Mirsky et al., 2019) experiment, the tumor injected misdiagnosis rate dropped from 99.2% to 70%, and though this improvement is drastic in terms of human performed detection, it is far greater than the misdiagnosis rate of deep transfer learning which is <1%. The monumental limitation of the method presented in this section is the singular focus on FM scans, which allowed for tumor site localization. Providing knowledge on where to look in a 512x512 scan eliminates the additional task of searching for countless possible tampering locations, drastically simplifying the problem. This method of localization cannot be performed on FB scans as the tumor site is unknown in a practical setting.

3.2 False Benign detection

The primary focus for this section is classifying FB from untampered scans, where tumors are removed. Unlike the previous section, we do not have the liberty of tumor site localization: the location of the region of interest is unknown in a practical setting.

3.2.1 Negative Space Reduction

Section 3.1.1 already covered classifier performance without any dimensionality reduction in a small testing sample. As shown in Table 2, ML model accuracy is on average approximately 44% higher than transfer learning. With this in mind, we reconduct the testing on scans from 3.1.1 with negative space reduction as a means for dimensionality reduction. Negative space refers to the zeroed pixels surrounding the ROI. Unlike Section 3.1.2, the ROI in this section is the entire lung. Each pixel array is sliced in a manner that isolated the lungs and visible nodules. This will preserve the delocalized image without removing any useful image features.

Classifier metrics for delocalized image data are presented in Table 5. SVM and Random Forest perform reliably given the small sample size by nature of machine learning algorithms. Certain non-deterministic features are easily extracted without the need for deep learning. Untampered recall is higher than tampered recall for most transfer learning models, indicating overcompensated predictions for the untampered class. This overcompensation is suspected to arise

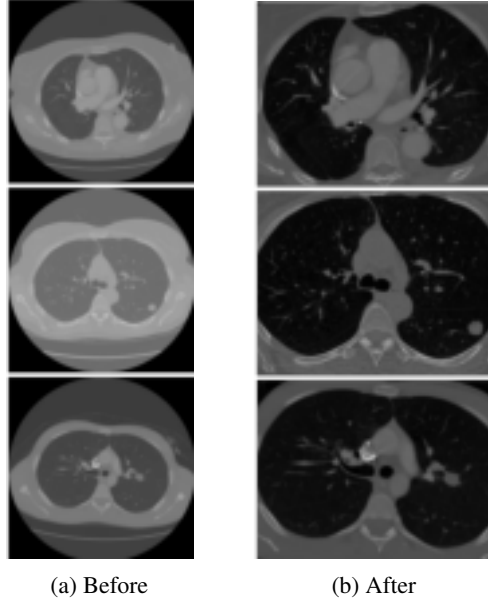


Figure 6: Negative space reduced scans
Row 1: FB samples, Row 2: FM samples, Row 3: Untampered samples

due to an unclear decision boundary between the FB and untampered classes: denoised malign tumor sites are absent in both. AUC scores in Figure 7 reflect excellent, poor, and failed scores for this task.

$$Precision = \frac{True\ Positives}{True\ Positives + False\ Positives} \quad (1)$$

$$Recall = \frac{True\ Positives}{True\ Positives + False\ Negatives} \quad (2)$$

Table 5: Delocalized image classifier performance

Classifier	Accuracy	untampered Precision	untampered Recall	tampered Precision	tampered Recall
SVM	1	1	1	1	1
Random Forest	0.96	0.9	1	1	0.938
Decision Tree	0.92	0.818	1	1	0.875
DenseNet121	0.594	0.467	0.583	0.706	0.6
DenseNet201	0.5	0.357	0.417	0.611	0.55
ResNet50	0.531	0.421	0.667	0.692	0.45
ResNet101	0.313	0.292	0.583	0.375	0.15
VGG19	0.406	0.316	0.5	0.538	0.35

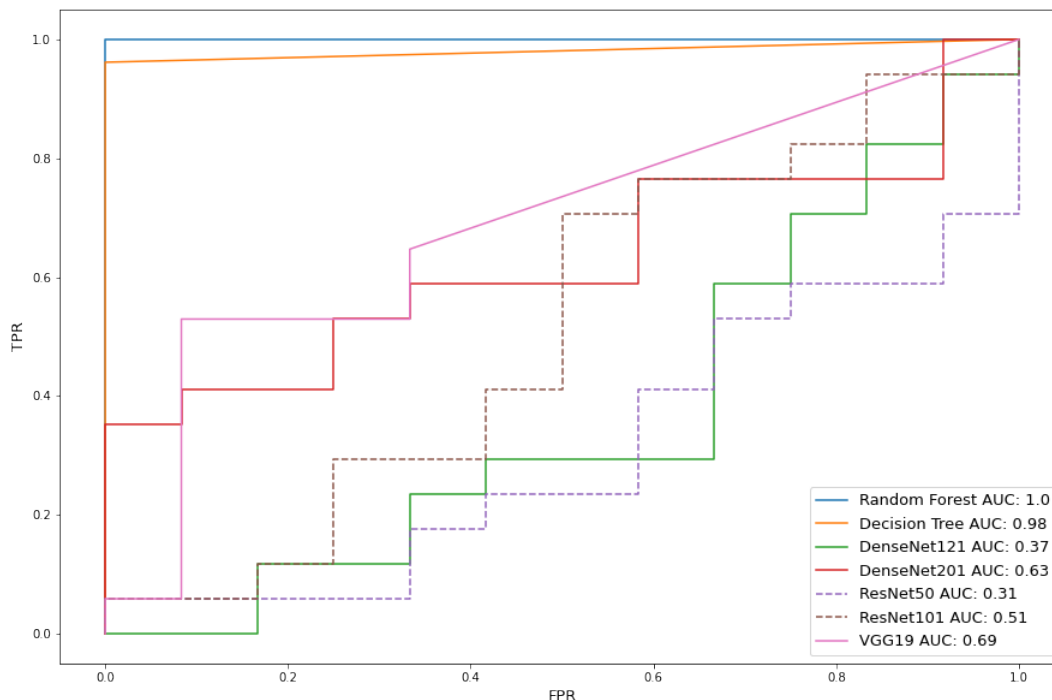


Figure 7: Delocalized image classifier ROC curves

3.2.2 Data Augmentation

Once again, we repeat the previous tests using data augmentation. In accordance with section 3.1.3, Table 6 shows data augmentation of CT scans does improve deep learning accuracy. Random forest performance is on par with ResNet101, showing the feature pool for 266x340 images could be more representative of the class boundaries when compared to localized 128x128 image slices. Mean accuracy by model, however, is lower by 0.0148%, equating to 15 additional misdiagnoses per 1000 scan classifications, confirming a larger feature pool is more difficult to learn efficiently. Perfect untampered precision and tampered recall scores, and lower untampered recall and tampered precision on SVM, DenseNet201, and ResNet50 indicate overcompensation on tampered predictions while correctly classifying 92% of untampered scans. Given perfect model accuracy is non-viable, this is the preferred scenario considering loss of life is more concerning than expense of resources. AUC scores in Figure 8 indicate excellent performance.

Table 6: Augmented delocalized image classifier performance

Classifier	Accuracy	untampered Precision	untampered Recall	tampered Precision	tampered Recall
SVM	0.959	1	0.919	0.925	1
Random Forest	0.987	0.998	0.977	0.977	0.998
Decision Tree	0.913	0.861	0.985	0.983	0.841
DenseNet121	0.962	0.935	0.993	0.992	0.931
DenseNet201	0.957	1	0.914	0.921	1
ResNet101	0.976	0.969	0.984	0.984	0.968
ResNet50	0.955	1	0.911	0.918	1
VGG19	0.933	0.886	0.995	0.994	0.872

The results of this section indicate the detection of FB scans can be done at high rates of accuracy and recall, accounting also for false negatives. In the open trial conducted by CT-GAN (Mirsky et al., 2019) researchers, where knowledge of the attack was known, attack success rates dropped a mere 5.8% from its initial 95.8%. With a very small margin of improvement arising from educating radiologists on attacks, this work emphasizes the room for improvement in state of the art AI frameworks that assist radiologists in making informed decisions.

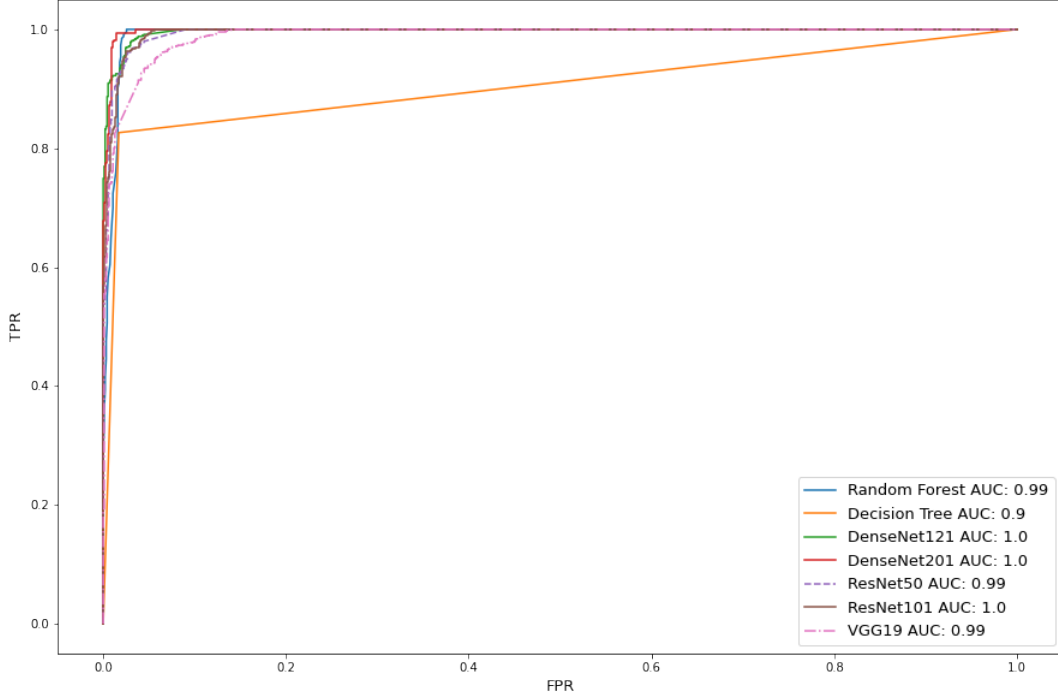


Figure 8: Augmented delocalized ROC curves

3.3 Multiclass Classification

In this section we test classification of delocalized untampered, FB, and FM images in 3 distinct classes rather than binary. FB and FM images are augmented in order to balance data quantity with the untampered class. Samples are identical to those provided in Figure 6. Multiclass classification results from Table 7 show overall untampered precision is significantly higher than FB and FM precision: indicating deep learning is best for drawing decision boundaries between the two classes. However, neither model type can consistently distinguish FM and FB. Most models have higher FM recall metrics than FB recalls while having little deviation between FB metrics. This leads FM to be the favored prediction of the two subtypes.

Table 7: Multiclass delocalized image classifier performance

Classifier	Accuracy	untamp. Precision	untamp. Recall	FB Precision	FB Recall	FM Precision	FM Recall
SVM	0.591	0.998	0.927	0.405	0.407	0.411	0.437
Random Forest	0.665	1	0.923	0.509	0.495	0.52	0.576
Decision Tree	0.641	0.769	0.936	0.548	0.45	0.559	0.537
DenseNet121	0.804	0.998	0.978	0.733	0.655	0.693	0.78
DenseNet201	0.777	0.993	0.925	0.687	0.561	0.651	0.814
ResNet50	0.641	1	0.923	0.492	1	0	0
ResNet101	0.706	0.97	0.974	0.557	0.584	0.592	0.561
VGG19	0.657	0.785	0.966	0.595	0.32	0.557	0.687

4 Conclusion

This paper tested various ML and DL models, as well as image isolation methods for GAN based tampering. We showed the detection of artificially generated deformities in medical imaging can be performed with high confidence. Based on the case studies, we found deep learning with localization of the region of interest to be most proficient at classifying tumor injected scans. The same can also be repeated with negative space reduced scans when localization is infeasible. Future works may involve training on hospital scans and integration of real time deep learning based tamper detection into PACS systems.

CRedit authorship contribution statement

Siddharth Solaiyappan: Conceptualization, Methodology, Software, Formal analysis, Investigation, Data Curation, Writing - Original Draft.

Yuxin Wen: Methodology, Writing - Review & Editing, Supervision

Conflict of Interest Statement

The authors have no conflicts of interest to declare. All co-authors have seen and agree with the contents of the manuscript and there is no financial interest to report. We certify that the submission is original work and is not under review at any other publication.

References

- A. P. Reeves, A. M. B. (2011). The Lung Image Database Consortium (LIDC) Nodule Size Report. <http://www.via.cornell.edu/lidc/>
- Armato III, S. G., McLennan, G., Bidaut, L., McNitt-Gray, M. F., Meyer, C. R., Reeves, A. P., Zhao, B., Aberle, D. R., Henschke, C. I., Hoffman, E. A., Kazerooni, E. A., MacMahon, H., Van Beek, E. J. R., Yankelevitz, D., Biancardi, A. M., Bland, P. H., Brown, M. S., Engelmann, R. M., Laderach, G. E., ... Clarke, L. P. (2015). Data From LIDC-IDRI [Data set]. The Cancer Imaging Archive. <https://doi.org/10.7937/K9/TCIA.2015.LO9QL9SX>
- Barragán-Montero, A. M., Thomas, M., Defraene, G., Michiels, S., Haustermans, K., Lee, J. A., & Sterpin, E. (2021). Deep learning dose prediction for imrt of esophageal cancer: The effect of data quality and quantity on model performance. *Physica Medica*, 83, 52–63. <https://doi.org/10.1016/j.ejmp.2021.02.026>
- Beck, C. (2018). McAfee researchers find poor security exposes medical data to cybercriminals. <https://www.mcafee.com/blogs/other-blogs/mcafee-labs/mcafee-researchers-find-poor-security-exposes-medical-data-to-cybercriminals/>
- Brunese, L., Mercaldo, F., Reginelli, A., & Santone, A. (2019). Radiomic features for medical images tamper detection by equivalence checking [Knowledge-Based and Intelligent Information & Engineering Systems: Proceedings of the 23rd International Conference KES2019]. *Procedia Computer Science*, 159, 1795–1802. <https://doi.org/10.1016/j.procs.2019.09.351>
- Bunk, J., Bappy, J. H., Mohammed, T. M., Nataraj, L., Flenner, A., Manjunath, B. S., Chandrasekaran, S., Roy-Chowdhury, A. K., & Peterson, L. (2017). Detection and localization of image forgeries using resampling features and deep learning. *2017 IEEE Conference on Computer Vision and Pattern Recognition Workshops, CVPR Workshops 2017, Honolulu, HI, USA, July 21-26, 2017*, 1881–1889. <https://doi.org/10.1109/CVPRW.2017.235>
- Clark, K., Vendt, B., Smith, K., Freymann, J., Kirby, J., Koppel, P., Moore, S., Phillips, S., Maffitt, D., Pringle, M., Tarbox, L., & Prior, F. (2013). The cancer imaging archive (TCIA): Maintaining and operating a public information repository. *Journal of digital imaging*, 26(6), 1045–1057. <https://doi.org/10.1007/s10278-013-9622-7>
- Cozzolino, D., Poggi, G., & Verdoliva, L. (2015). Efficient dense-field copy-move forgery detection. *IEEE Trans. Inf. Forensics Secur.*, 10(11), 2284–2297. <https://doi.org/10.1109/TIFS.2015.2455334>
- Dua, D., & Graff, C. (2017). UCI machine learning repository. <https://archive.ics.uci.edu/ml/datasets>
- El Khouli, R. H., Macura, K. J., Barker, P. B., Habba, M. R., Jacobs, M. A., & Bluemke, D. A. (n.d.). Relationship of temporal resolution to diagnostic performance for dynamic contrast enhanced mri of the breast. *Journal of Magnetic Resonance Imaging*, 30(5), 999–1004. <https://doi.org/10.1002/jmri.21947>
- El-Latif, A., E.I., Taha, A., & Zayed, H. (2020). A passive approach for detecting image splicing based on deep learning and wavelet transform. *Arabian Journal for Science and Engineering*, 45. <https://doi.org/10.1007/s13369-020-04401-0>
- Isola, P., Zhu, J.-Y., Zhou, T., & Efros, A. A. (2016). Image-to-image translation with conditional adversarial networks. *CoRR, abs/1611.07004*. <http://arxiv.org/abs/1611.07004>
- Liao, F., Liang, M., Li, Z., Hu, X., & Song, S. (2017). Evaluate the malignancy of pulmonary nodules using the 3d deep leaky noisy-or network. *CoRR, abs/1711.08324*. <http://arxiv.org/abs/1711.08324>
- Meena, K. B., & Tyagi, V. (2020). A copy-move image forgery detection technique based on tetrolet transform. *J. Inf. Secur. Appl.*, 52, 102481. <https://doi.org/10.1016/j.jisa.2020.102481>
- Mirsky, Y., Mahler, T., Shelef, I., & Elovici, Y. (2019). CT-GAN: malicious tampering of 3d medical imagery using deep learning. *CoRR, abs/1901.03597*. <http://arxiv.org/abs/1901.03597>
- Mohammed, A. A., Jebur, B. A., & Younus, K. M. (2021). Hybrid DCT-SVD based digital watermarking scheme with chaotic encryption for medical images. *IOP Conference Series: Materials Science and Engineering*, 1152(1), 012025. <https://doi.org/10.1088/1757-899x/1152/1/012025>

- Pedregosa, F., Varoquaux, G., Gramfort, A., Michel, V., Thirion, B., Grisel, O., Blondel, M., Prettenhofer, P., Weiss, R., Dubourg, V., Vanderplas, J., Passos, A., Cournapeau, D., Brucher, M., Perrot, M., & Duchesnay, E. (2011). Scikit-learn: Machine learning in Python. *Journal of Machine Learning Research*, 12, 2825–2830.
- Rao, Y., & Ni, J. (2016). A deep learning approach to detection of splicing and copy-move forgeries in images. *IEEE International Workshop on Information Forensics and Security, WIFS 2016, Abu Dhabi, United Arab Emirates, December 4-7, 2016*, 1–6. <https://doi.org/10.1109/WIFS.2016.7823911>
- Savaridass, M. P., Deepika, R., Aarnika, R., Maniraj, V., Gokilanandhi, P., & Kowsika, K. (2021). Digital watermarking for medical images using DWT and SVD technique. *IOP Conference Series: Materials Science and Engineering*, 1084(1), 012034. <https://doi.org/10.1088/1757-899x/1084/1/012034>
- School, H. M. (2020). Radiation risk from medical imaging. *Harvard Health Publishing*. <https://www.health.harvard.edu/cancer/radiation-risk-from-medical-imaging>
- Setio, A. A. A., Traverso, A., de Bel, T., Berens, M. S. N., van den Bogaard, C., Cerello, P., Chen, H., Dou, Q., Fantacci, M. E., Geurts, B., van der Gugten, R., Heng, P.-A., Jansen, B., de Kaste, M. M. J., Kotov, V., Lin, J. Y.-H., Manders, J. T. M. C., S'onora-Mengana, A., Garc'ia-Naranjo, J. C., ... Jacobs, C. (2016). Validation, comparison, and combination of algorithms for automatic detection of pulmonary nodules in computed tomography images: The LUNA16 challenge. *CoRR*, abs/1612.08012. <http://arxiv.org/abs/1612.08012>
- SG, A. 3., G, M., L, B., MF, M.-G., CR, M., AP, R., B, Z., DR, A., CI, H., EA, H., EA, K., H, M., EJ, V. B., D, Y., AM, B., PH, B., MS, B., RM, E., GE, L., ... BY., C. (2011). The lung image database consortium (LIDC) and image database resource initiative (IDRI): A completed reference database of lung nodules on CT scans. *Medical Physics*, 38, 915–931. <https://doi.org/10.1118/1.3528204>
- T., S., K., S., M., U., & K., O. (2021). Computed tomography. *Transparency in Biology*. Springer, Singapore. https://doi.org/10.1007/978-981-15-9627-8_8